

Integration of Ruthenium oxide-Carbon Nanotube Composites with Three-Dimensional Interdigitated Microelectrodes for the Creation of On-Chip Supercapacitors

Yajiang Yin, Xiaofeng Wang*, Zheng You

Department of Precision Instrument, Tsinghua University, No.1 Tsinghua Yuan, Haidian District, Beijing, P. R. China

*E-mail: xfw@tsinghua.edu.cn

Received: 22 February 2017 / Accepted: 19 March 2017 / Published: 12 April 2017

A three-dimensional (3D) on-chip supercapacitor is fabricated by performing deep-ultraviolet lithography on a SU-8 photoresist. By using a cathodic deposition technique, ripple-like ruthenium oxide-carbon nanotube nanocomposites are synthesized. The carbon nanotube (CNT) network in the nanocomposite makes the electrolyte penetration easier and facilitates proton exchange and diffusion. A specific capacitance of $208.5 \text{ mF}\cdot\text{cm}^{-2}$ is achieved at $10 \text{ mV}\cdot\text{s}^{-1}$ in a neutral Na_2SO_4 solution. The interdigitated cell forms a supercapacitor when it is placed on a chip, and exhibits many desirable properties; the specific capacitance of as high as $28.70 \text{ mF}\cdot\text{cm}^{-2}$ is achieved at $120 \text{ mA}\cdot\text{cm}^{-2}$. The highest energy density ($25.99 \text{ mJ}\cdot\text{cm}^{-2}$) and the highest power density ($46.92 \text{ mW}\cdot\text{cm}^{-2}$) are also achieved with the interdigitated micro-supercapacitor. Therefore, 3D microstructures made with electrochemically deposited carbon nanotube composites are promising candidates for application as on-chip supercapacitors.

Keywords: On-chip supercapacitor; Ruthenium oxide; Carbon nanotubes; Interdigitated microstructures; Micro-electro-mechanical systems.

1. INTRODUCTION

The rapid development of micro-electro-mechanical systems (MEMS) and microelectronic devices follows a trend of miniaturization. Increasing attention has been given to microsystems with integrated sensors, actuators and control circuits, which have applications in various areas such as the automotive and microelectronics industries, in space exploration, biomedicine and healthcare [1]. Advances in the fields of micro and nanoscale fabrication have inspired the development of micro-power sources, which have the potential to be integrated into small electronic devices. Several types of

micro-sized power sources, such as micro batteries [2,3], microscale fuel cells [4,5], micro-supercapacitors [6,7] and energy harvesters [8,9], have been developed in recent years. Among these, microscale batteries are the most promising power sources because they display a relatively high energy density. However, when integrated into systems that are hard to access, the limited life span of these batteries becoming a big issue due to the difficult maintenance and replacement. Moreover, micro-batteries are ineffective when it comes to low-temperature or high-power applications like wireless transmission. Micro-supercapacitors can be coupled with micro batteries and energy harvesting microsystems to provide high peak power, long cycle lives, and high charge/discharge rates. Furthermore, micro supercapacitors with high energy densities can serve as stand-alone and maintenance-free power sources in various types of microsystems.

Two types of supercapacitors exist and they are categorized based on their mechanism of action: (a) electric double layer capacitors and (b) pseudocapacitors. Electric double layer capacitors (EDLCs) store energy via ion adsorption. Pseudocapacitors store energy via fast redox reactions between the electroactive materials on the electrode surface and the electrolyte. The principles mentioned above also apply to micro-supercapacitors, which are different in their structural design and ionic diffusion behavior [10,11]. Recent efforts have focused on increasing the energy and power densities of micro supercapacitors by improving the properties of the materials utilized and the architecture of the devices [12-14]. Increases in power density can be achieved by decreasing the spacing between adjacent electrodes. Most on-chip micro supercapacitors have an interdigitated structure [15-20]. Besides, their electrodes can also be designed into sandwich and roll-like architectures [21]. For this kind of devices, most of their specific capacitances that have been reported in the literature were normalized to the Euclidean area of the electrodes other than the mass of the active materials. Xiong and Fisher [22] have comprehensively reviewed the research about the fabrication of on-chip micro supercapacitors. The interdigitated architecture is also advantageous when there is a limited area (e.g., when micro-supercapacitors are placed onto integrated circuit chips). Supercapacitors with interdigitated architectures are cost effective for mass production, in which case establishing layers of functionality is required.

The specific capacitance and energy density of a micro-supercapacitor can be increased by improving the electrochemical performance of the active materials in a given footprint area. Similar to their more conventional counterparts, micro-supercapacitors are generally constructed from two main types of materials: (i) carbon materials with high specific surface areas and (ii) polymers and metal oxides with high pseudocapacitances. Early reports discussed micro-supercapacitors that were based on pseudo-capacitive polymers (e.g., polypyrrole (PPy)) that were directly coated on current collectors that were pre-patterned using conventional lithography techniques. Sung et al. fabricated solid state electrochemical microcapacitors using a combination of photolithography and electrochemical polymerization [23]. These structures had a specific capacitance of $2 \text{ mF}\cdot\text{cm}^{-2}$. Sun reported a micro-supercapacitor with an interdigitated PPy electrode architecture through electrochemical fabrication, which has a geometric capacitance and a specific power of $29 \text{ mF}\cdot\text{cm}^{-2}$ and $2.2 \text{ mW}\cdot\text{cm}^{-2}$, respectively [24]. These architectures can be easily made using this method because PPy is electropolymerizable and electrically active in aqueous media.

Some literatures have reported micro-supercapacitors using ruthenium oxide pseudo-capacitive materials. A type of micro supercapacitor consisting of hydrous RuO₂ interdigitated electrodes has been reported by Liu et al., which exhibited a specific capacitance of 10.5 mF·cm⁻² at 50 mV·s⁻¹ [25]. However, the capacitances of the devices in the studies mentioned above decrease fast at higher scan rates, which is due to the high internal resistance and limited surface area of the planar electrode. Arnold et al. utilized laser direct-writing and micromachining to construct hydrous ruthenium oxide micro supercapacitors with high capacity [26], which has a specific capacitance that is comparable to the analogous reported values (720 F·g⁻¹). Sugimoto et al. have fabricated RuO_x electrodes using an electrodeposition method involving a lyotropic liquid crystal template [27]. The interdigitated array electrodes have ordered mesoporous RuO_x, which results in a specific capacitance of 400 F·g⁻¹. Ponrouch prepared Pt@RuO₂ core shell nanotube arrays by electrodepositing RuO₂ on Pt nanotubes and evaluated these structures as micro-supercapacitor electrodes [28]. The specific geometric capacitance of the RuO₂ core-shell nanotube electrodes was 320 mF·cm⁻² at 2 mV·s⁻¹ and 256 mF·cm⁻² at 500 mV·s⁻¹, indicative of the high utilization factor of the RuO₂ resulting from the facilitated proton and electron transport. Hu et al. synthesized hydrous RuO₂ tubular array electrodes using an anodic deposition technique [29]. The annealed RuO₂·H₂O nanotubes have a specific power and energy density of 4320 kW·kg⁻¹ and 7.5 Wh·kg⁻¹, respectively; thus, they are promising as a type of next-generation micro supercapacitor. Wang et al. prepared tubular ruthenium oxide by cathodically depositing RuO₂ on Si with grass-like prominence and evaluating these structures as micro-supercapacitor electrodes [30]. These devices gave a specific capacitance of 99.3 mF·cm⁻² at 5 mV·s⁻¹ in neutral Na₂SO₄ solution. The energies and power densities of micro-supercapacitors can be increased by using pseudo-capacitive ruthenium oxide. However, faradaic reactions are confined to the outermost layer of the system, and a large portion of the underlying RuO₂ remains unreacted. To achieve highly electro-active films on the microelectrode surfaces that are optimized for micro-supercapacitor applications, new fabrication techniques are highly needed.

Carbon materials with high surface areas and large pore sizes have been extensively investigated as electrode materials in micro supercapacitor systems [31]. Pech et al. used an ink jet to print activated carbon powder on interdigitated gold current collectors [32], producing micro supercapacitors with a 27 mF·cm⁻² geometric capacitance. Efforts have been made to increase the energy and power densities of such electrodes in recent years by employing novel three-dimensional (3D) architectures. Shen et al. prepared microelectrodes by filling etched, interdigitated channels on substrates with an activated carbon slurry (50 μm thick); this device exhibited a much higher area-normalized capacitance of 90.7 mF·cm² and a power density of 51.5 mW·cm² [33]. Xing et al. fabricated a micro supercapacitor and injected a carbon suspension into its interdigitated channels using photoresist as the separator. The supercapacitor exhibited a high specific energy (330 mJ·cm⁻²) and a large specific capacitance (160 mF·cm⁻²) [34]. Beidaghi et al. reported a type of micro-supercapacitor with activated C-MEMS structures, which exhibited specific capacitances of up to 75 mF·cm⁻² at 5 mV·s⁻¹ after electrochemical activation [35]. By uniformly coating pseudocapacitive PPy onto the C-MEMS architectures, the energy density of this micro capacitor was further improved [36]. Electrochemical characterization revealed that these micro-capacitors could deliver a specific capacitance of 162.07 mF·cm⁻² at 20 mV·s⁻¹. Recent advances in the design and fabrication of C-

MEMS microcapacitors have been thoroughly reviewed by Beidaghi and Wang [37]. Because currently it is complicated to construct such 3D structures, especially those with good mechanical stability, it is reasonable to conclude that designing 3D electrode structures for use as micro-supercapacitors will be an active area of interest in the future.

CNTs (carbon nanotubes) are of great interest as electrode materials in conventional supercapacitors because of their unique structure, high surface area, low mass density, outstanding chemical stability and excellent electrical conductivity. To date, there are some studies involving CNT-based micro supercapacitors, which have a common problem that these CNT-based materials are difficult to bond to the substrate. When wetted by an aqueous electrolyte, the CNTs detach from the substrate, resulting in poor cyclic stability [22]. Moreover, since the CNTs are not strongly bonded to the supporting metal, the internal resistance in such devices tends to be large. The CNTs can be filled with additional conducting polymers or oxides to achieve good electrical conductivity and mechanical robustness. Jiang et al. fabricated a double-layer symmetric supercapacitor, utilizing vertically aligned CNT forests (80 μm in height) on silicon wafers, that had a capacitance density of $428 \mu\text{F}\cdot\text{cm}^{-2}$ and a low power density of $0.28 \text{ mW}\cdot\text{cm}^{-2}$ [38]. Liu et al. built asymmetric micro supercapacitors with planar configurations. Vertically aligned CNTs added with manganese oxide were fabricated on the interdigitated array electrodes [39]. The relatively high resistance of the CNTs and the MnO_2 -CNTs resulted from their rapidly decreasing capacitance values as the sweep rate increased, although each CNT finger was approximately 34 μm thick. To increase the specific capacitance and energy density of micro supercapacitors, it is preferable that the increase of the thickness of the active materials does not sacrifice the cyclic stability and power densities.

This work introduces a versatile and effective approach geared toward enhancing the energy and power density of microcapacitor devices by combining a high-aspect ratio, interdigitated 3D microstructure and a high capacitance, porous RuO_2/CNT nanocomposite. Deep ultraviolet (UV) lithography techniques employing a SU-8 photoresist were utilized to fabricate 3D current collectors in these micro supercapacitors. The ruthenium oxide and carbon nanotubes were electrochemically deposited simultaneously in the 3D interdigitated microstructure to form a capacitive micro cell. The robust SU-8 microstructure was used as the supporter and separator for growing a capacitive film with a thickness as great as 40 μm . A ripple-like CNT-based nanocomposite film was fabricated by in situ electrodeposition onto the above-mentioned structure. The electrochemical performance of both the microelectrodes and the entire symmetric cells were measured by cyclic voltammetry and galvanostatic charge–discharge experiments. Active nanocomposites with well-designed 3D architectures and high electronic conductivities are needed for the fabrication of high capacitive microelectrodes and high performance micro-supercapacitors.

2. EXPERIMENTAL METHODS

2.1 Design of the micro-supercapacitor

Fig. 1(a) shows a schematic of an on-chip micro supercapacitor with 3D interdigitated electrodes placed on current collectors. In this architecture, the interdigitated anode and cathode were

fabricated on the same glass substrate. The CNT nanocomposite was separated and surrounded by SU-8 photoresist. The 3D interdigitated structure not only allows short circuits to be avoided but also provides mechanical support for the electrodes, which are often thick. The total footprint area of a typical sample was about 5mm^2 ($2.7\text{ mm} \times 1.85\text{ mm}$), as shown in Fig.1(b); each sample typically had a total of 14 interdigitated fingers (seven fingers for each electrode). Each finger of the microstructure (and thus each finger of the electrode) was $100\text{ }\mu\text{m}$ wide and $40\text{ }\mu\text{m}$ deep. The SU-8 separator between the interdigitated fingers was $100\text{ }\mu\text{m}$ wide. Advantageously, the above mentioned 3D interdigitated architectures minimize the diffusion path the of electrolyte ions between the electrodes and also increase the effective surface area of each electrode in the footprint area of the device.

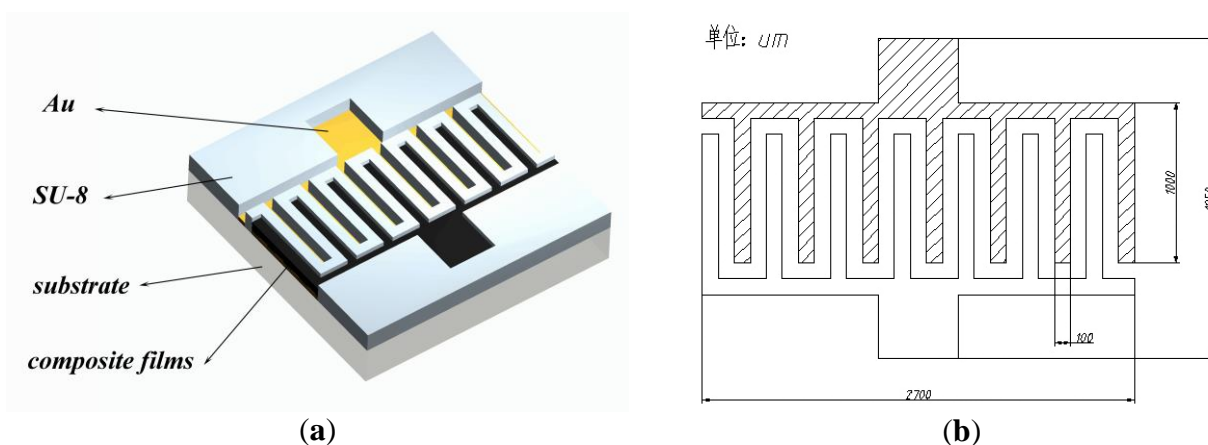


Figure 1. Schematic diagram of the on-chip micro-supercapacitor. (a) Device structure of micro-supercapacitor; (b) Planar design of interdigitated electrodes.

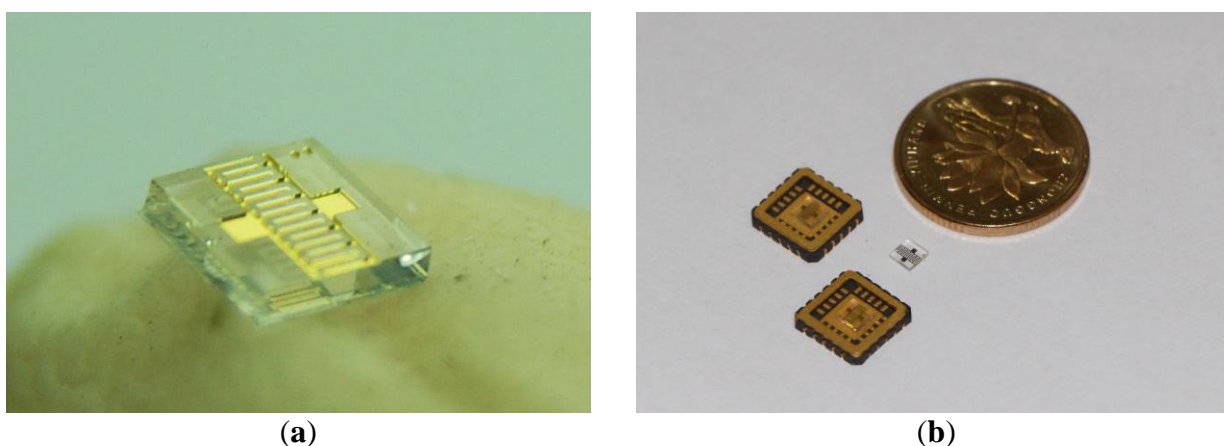


Figure 2. Photos of a 3D micro-supercapacitor (a) cell and (b) packaged prototype.

Fig. 2 shows photos of (a) a cell and (b) a packaged prototype. Briefly, the fabrication process involves the following steps: Step 1 involves sputtering a $40\text{ nm}/120\text{ nm}$ Ti/Au layer on a glass wafer, as shown in Fig. 3a. Step 2 involves applying lithography and etching to form interdigitated current

collectors as shown in Fig. 3b. Step 3 involves spin coating a SU-8 layer on the Ti/Au, which is then exposed by UV light; then, the unexposed SU-8 is removed as shown in Fig. 3c. Step 4 involves electro depositing the CNT nanocomposite into the fingers formed by the SU-8, as shown in Fig. 3d. This prototype was then packaged in a ceramic envelope and neutral Na_2SO_4 electrolyte is injected in the effective area.

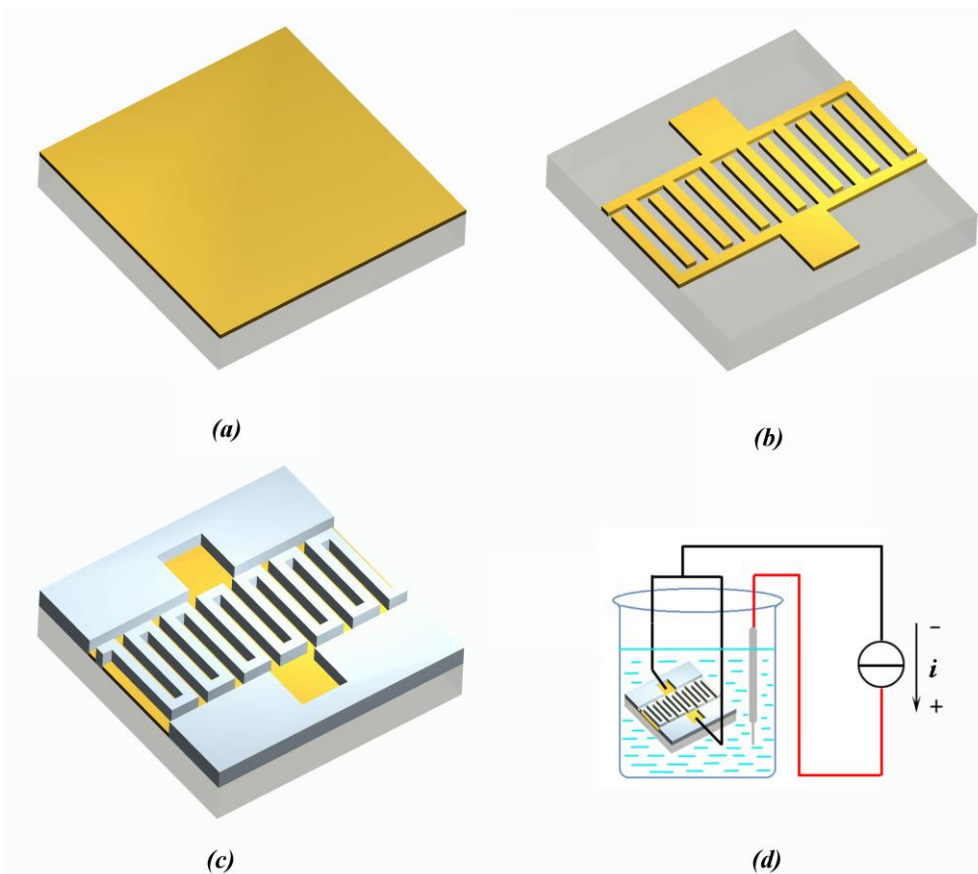


Figure 3. The fabrication process for a 3D micro-supercapacitor. (a) Sputtering a Ti/Au layer on a glass wafer, (b) Forming an interdigitated metal current collector, (c) Fabricating an interdigitated SU-8 microstructure, (d) Filling the CNT composite by electrodeposition.

2.2 Construction of the 3D MEMS structures

In this paper, UV lithography was performed on a SU-8 negative photoresist to fabricate interdigitated channels that could be used for supporting thick electrodes. The detailed procedure that was used for fabricating these 3D structures is described briefly. First, a 160-nm-thick Ti/Au layer with an interdigitated pattern is deposited on a clean glass substrate using radio-frequency (RF) sputtering and lithography techniques. Afterward, a SU-8 layer was uniformly spin-coated on the Ti/Au layer using a CHEMAT KW4-A (China) and then baked at 65°C and 95°C for 10 and 30 min, respectively, in a leveled oven. Next, the SU-8 layer was exposed to UV light using a SUSS MA 6 (Germany) and baked at 65°C and 95°C for 10 and 20 min, respectively. Finally, the unexposed SU-8 was removed, and the remaining patterned SU-8 was hardened at 150°C for 60 min to form the desired 3D structure.

2.3 Fabrication of the ruthenium oxide and CNT-based nanocomposite

The multi-walled CNTs were synthesized by using a classical catalytic decomposition method, which were then purified by reflux in concentrated nitric acid. All the other reagents, including the ruthenium chloride (RuCl_3), were analytical grade and used as received. The purified CNTs (1 g), ruthenium chloride (RuCl_3 , 0.05 g) and sodium nitrite (NaNO_2 , 0.85 g) were dispersed in 50 mL of deionized water and sonicated for 30 min so that the Ru^{+3} were uniformly adsorbed on the CNTs. The CNT nanocomposites were added to the interdigitated micro structure by electrodeposition. The two electrodes of each device were connected, and then the device was utilized as the working electrode in an electrochemical cell (Fig. 3d). The platinum wires were used as both the reference and the counter electrodes. The CNT nanocomposites were fabricated on the MEMS current collectors using the above mentioned electrolyte solution at $500 \text{ mA}\cdot\text{cm}^{-2}$ for 2000 seconds. The prepared film was rinsed and dried at 80°C for approximately 10 min. All of the samples were subjected to voltammetric charge/discharge cycles (>1500) at a scan rate of $80 \text{ mv}\cdot\text{s}^{-1}$ prior to other experimental investigations to exclude the effect of the leakage current on the calculation of the capacitance for the single electrodes. Electrochemical synthesis enables not only the production of CNT nanocomposites but also their deposition onto complex substrates. To make comparison, a microelectrode loaded with the same amount of ruthenium oxide was synthesized using the same electrodeposition process into the same 3D microstructure. The distinct advantages of CNT nanocomposite was verified through the investigation of the surface topography and electrochemical performance of the film.

The mechanism of formation of RuO_2 from a RuCl_3 precursor is very complicated. Cathodic electrosynthesis is similar to amorphous oxide powder processing (a wet chemical method) in that it uses an electrogenerated base [40, 41]. In the preparation of RuO_2 , starting from $\text{RuCl}_3\cdot n\text{H}_2\text{O}$ via electrosynthesis, 3^+ metal ions are oxidized to the 4^+ state [40]. X-ray analyses revealed deposits containing significant amounts of both amorphous and hydrous phases with remarkable capacitive energy storage properties [41]. For simplicity, RuO_2/CNT is used in the following text to represent the active substance on the microstructure surface.

2.4 Characterization methods

The electrochemical properties of the CNT nanocomposites on the electrode surface were investigated by cyclic voltammetry (CV) and galvanostatic charge/discharge (GCD). A potentiostat/galvanostat (660B, CHI instrument, China) using both three-electrode and two-electrode systems in $0.1 \text{ mol}\cdot\text{L}^{-1}$ aqueous Na_2SO_4 electrolyte was applied to test the electrochemical test. A single micro electrode acted as the working electrode in the three-electrode system, and a Pt sheet and a saturated calomel electrode (SCE) acted as the counter and reference electrodes, respectively. Two MEMS electrodes acted as the working and the counter electrodes in the two-electrode system, respectively. All of the potentials discussed below are based on the reference voltage for the SCE. A scanning electron microscope (SEM FEI, Sirion 200, The Netherlands) and a transmission electron microscope (TEM JEM, JEM-1400, Japan) was used to study the microstructure and surface topography of the MEMS electrodes. The electrically active layer in the 3D microstructure was

characterized by the energy dispersive spectroscopy (EDS). The crystalline structure of the electrodes was characterized using an X-ray diffractometer. The X-ray diffraction (XRD) patterns were measured by a Cu K radiation system (60 kV, 80 mA, Bruker AXS D8 Discover, Germany).

3. RESULTS AND DISCUSSION

3.1 SEM imaging and XRD patterning

Fig. 4 shows the surface topography of the three-dimensional microstructure. The surface of the 3D microstructure was smooth, and the patterned SU-8 layer bonded well to the glass substrate (bulges did not protrude). Interdigitated electrode patterns were typically confined to a 5 mm^2 area, and the spacing between electrodes was $100 \text{ }\mu\text{m}$; such patterns were readily achieved using well-developed photolithography processes. The SU-8 photoresist is ideally suited for patterning high-aspect ratio structures with nearly vertical sidewalls. SU-8 is insulating and chemically stable, and it provides considerably strong mechanical support when cross-linked [34]. The surface topography of the ruthenium oxide electrodeposited for 2000 s in one electrode is shown in Fig. 5. For comparison, the other interdigitated electrodes on the chip do not contain ruthenium oxide. The deposited ruthenium oxide film is less than $5 \text{ }\mu\text{m}$ thick (much less than the height of the SU-8 separator). A higher magnification image taken from the surface of this electrode finger (Fig. 6) revealed a nanostructured granular morphology (average grain size between 30 and 50 nm) that is typical of electrodeposited ruthenium oxide. Because the active materials are confined to the bottoms of the cavities, we can expect longer diffusion lengths and thus higher resistance during ion transport; we can also expect a lower capacitance because only a small amount of substance is present. This problem can be solved in a number of ways. Although the deposition time could be increased up to 3000 seconds or longer, the excessively thick coating that would be formed may cause the RuO_2 films to detach as shown in Fig. 7. To increase the capacitance of the micro device without compromising its stability and achievable power, it is crucial to increase the thickness and conductivity of the 3D interdigitated electrode.

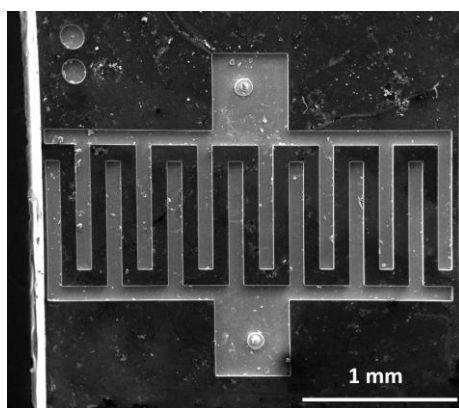


Figure 4. The surface topographies of 3D microstructures with interdigitated patterns.

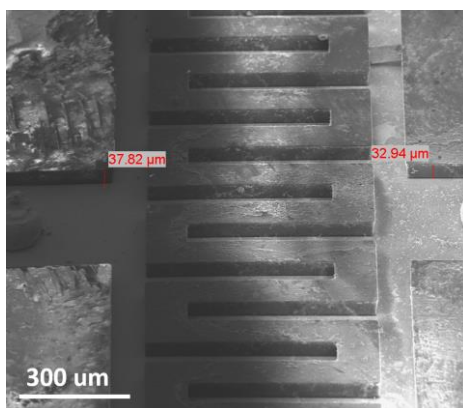


Figure 5. The surface topographies of microelectrodes (electrodeposited and untreated).

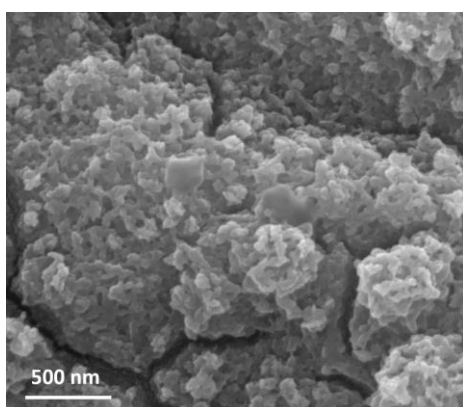


Figure 6. A SEM image of ruthenium oxide electrodeposited for 2000 seconds.

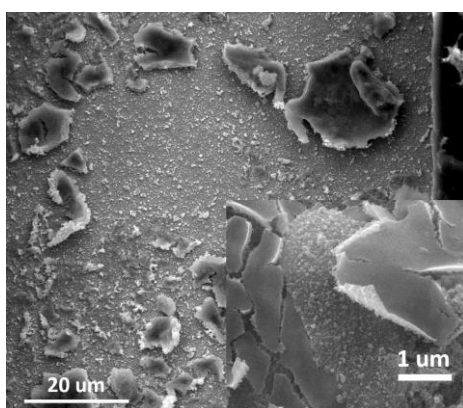


Figure 7. A SEM image of ruthenium oxide electrodeposited for 3000 seconds

The surface topography, capacitance and deposition efficiency of the functional film can be improved by integrating new carbon nanomaterials, such as CNTs, into micro-supercapacitors. The surface topography of the CNT nanocomposite in the finger of an SU-8 microstructure is presented in Fig. 8. The entire finger was uniformly filled with a thick layer of the CNT nanocomposite, which has unique porous and ripple-like morphology. The thickness of the nanocomposite was approximately 40

μm . A high-magnification image of the nanocomposite showed that the network of underlying CNTs was homogeneously covered with nanoparticles (Fig. 9). The microstructure of the SU-8 plays an important supporting role in the formation of these high-aspect ratio 3D electrodes.

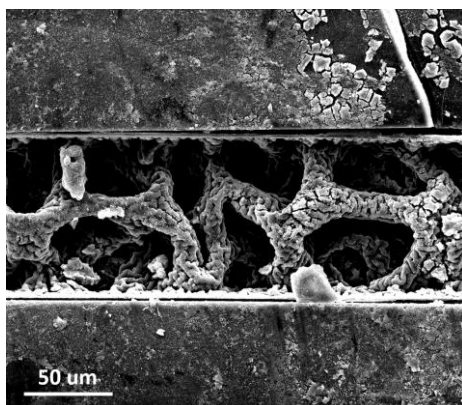


Figure 8. The surface topography of a microelectrode filled with CNT nanocomposite.

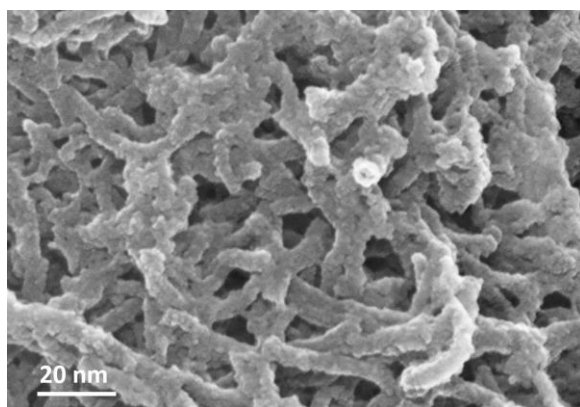


Figure 9. A SEM image of the CNT nanocomposite electrodeposited for 2000 seconds.

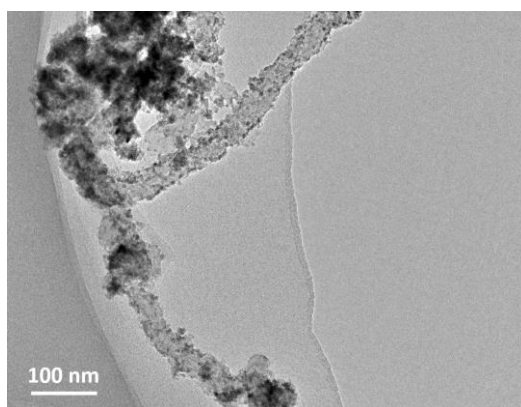


Figure 10. A TEM image of CNTs covered with ruthenium oxide nanoparticles.

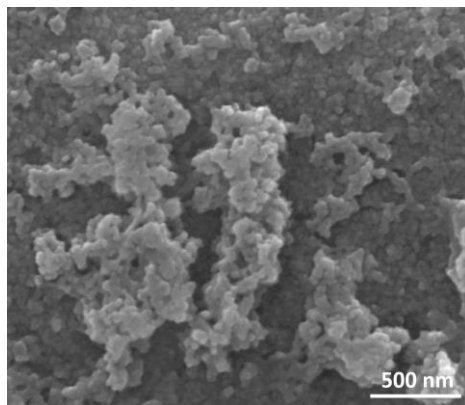


Figure 11. A SEM image of the CNT composite electrodeposited on a planar surface.

Fig. 10 shows a typical TEM image of the RuO_2/CNT nanocomposite. It can be seen that there is a high surface coverage of remarkably uniform ruthenium oxide nanoparticles. Well-dispersed ruthenium oxide nanoparticles were loaded onto each CNT, which binds the coated tubes into a porous 3D network. These CNTs not only were directly used as electrodes but were also used as nanotemplates for the pseudocapacitive RuO_2 materials. These CNTs allowed the deposition efficiency to be increased and the cyclic problem associated with volume swelling during long time electrodeposition processes to be solved. For comparison, a SEM micrograph of an electrochemically deposited nanocomposite on a planar surface is shown in Fig. 11. The CNTs grew at a low density and were randomly scattered over the surface.

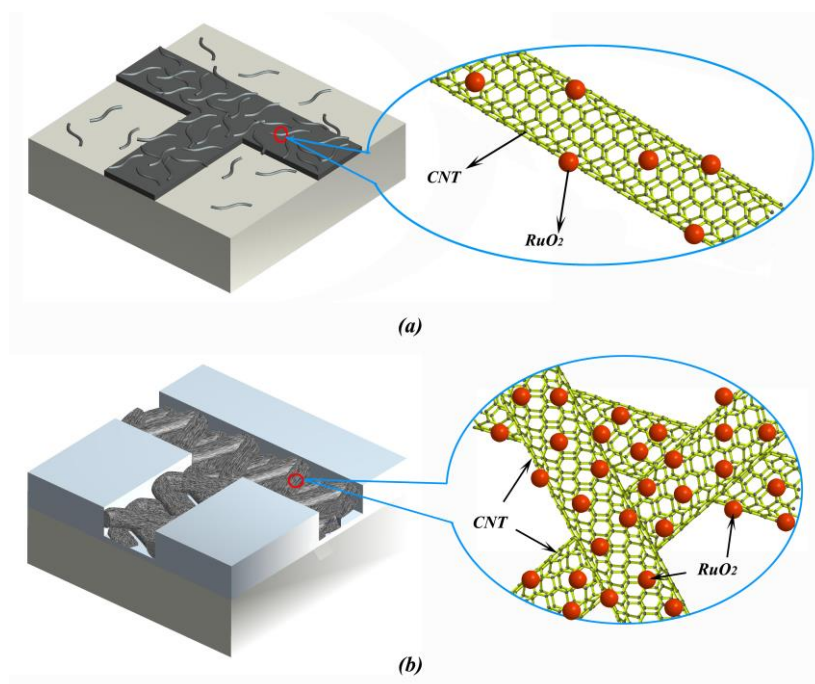


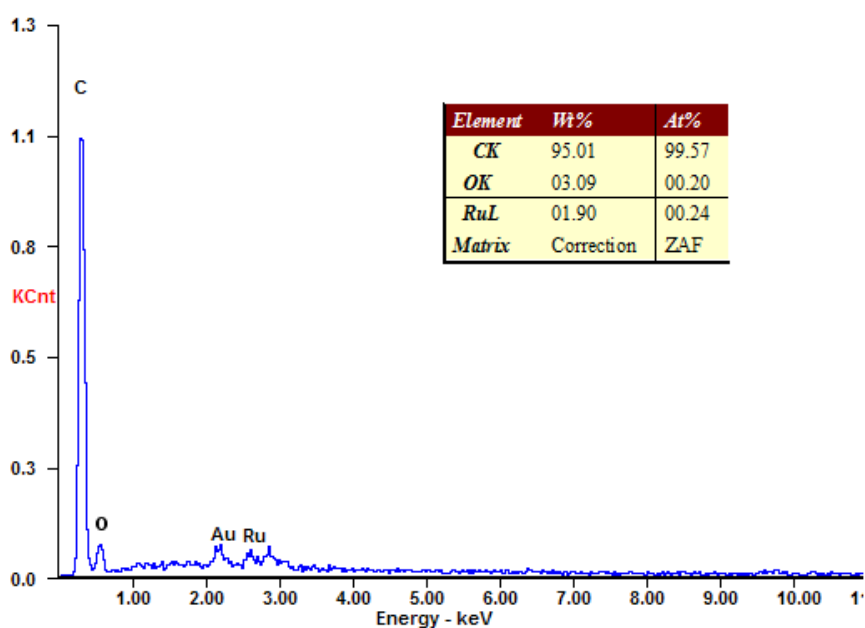
Figure 12. A schematic of the desired CNT nanocomposite structure (a) on a planar surface and (b) in a 3D microstructure.

Taken together, these electron microscopy images prove the importance of the presence of the 3D microstructure in the CNT nanocomposite film. It has been mentioned above that there is a common problem about using CNTs as electrode materials for micro-supercapacitors, which is that they often detach from the substrates. The smooth Au layer was supposed to impede the adhesion of the CNTs, and the cause of failure is shown in Fig. 12a. The CNTs could not effectively adhere to the flat and smooth surface without the support of a micro-spatial structure because the system was being stirred at high speed.

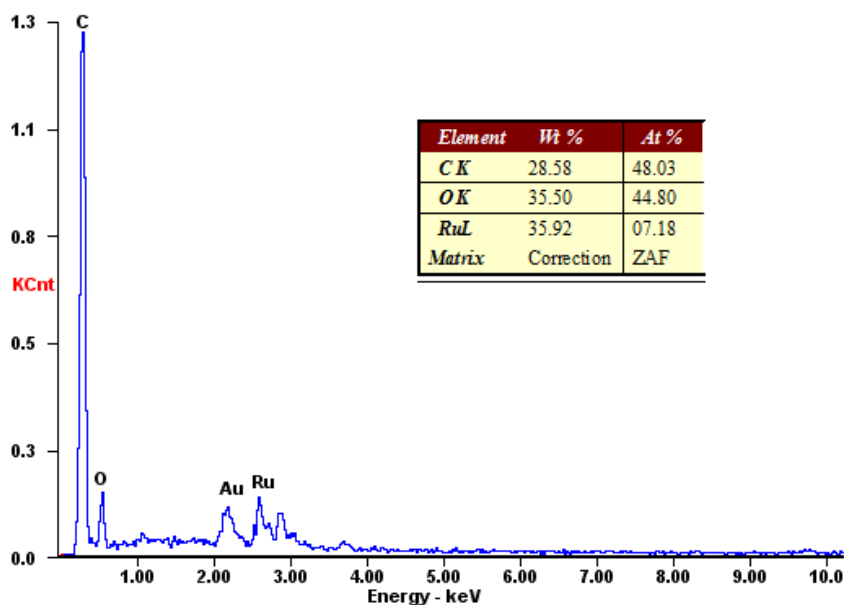
A schematic of the growth process of a nanocomposite with the desired 3D microstructure is illustrated in Fig. 12b. When the CNTs were supported by the 3D microstructure, the ruthenium oxide material could be deposited without disturbing them. Based on these data, we managed to increase the thickness of the active materials by a new method, which does not sacrifice the cyclic stability and power density of the micro-supercapacitor. We are confident that the use of a 3D microstructure is important for improving the capacitive characteristics of on-chip micro-supercapacitors.

The improved ionic conductivity, capacitance, and rate of response of the device are attributed to the structure of the composite film (Fig. 12b). First, the large surface area of porous RuO₂ allowed the electrolyte three-dimensional access. Second, because a thin layer of RuO₂ was coated on each CNT, the ion intercalation distance was on the order of nanometers. Finally, the conductivity of the composite was increased via the addition of the electrically conductive CNTs. In the following, the special electrochemical effects benefit from this distinctive structure will be discussed.

EDS indicated that the nanocomposite film with a ripple-like morphology was comprised of elemental oxygen, ruthenium and carbon (Fig. 13a), primarily from the CNT network. In particular, the weight percent of carbon in the film was as high as 95% after a deposition time of 2000 seconds. Thus, the nanocomposite film was almost entirely composed of carbon nanotubes.



(a)



(b)

Figure 13. EDS of the CNT nanocomposite electrodeposited for 2000 s. (a) On a planar surface, (b) In a 3D microstructure.

Compared with the RuO_2/CNT composite in 3D electrode, the weight percent of carbon for the film deposited on flat surface was only 28.58% (Fig. 13b). The data above has been verified experimentally using electron microscopy (Fig.11). Electrodeposition in 3D microstructure is an effective method for preparing a thick film composed mainly of CNTs that can be used in the fabrication of a 3D microelectrode. In this study, electrosynthesis allowed porous carbon materials to be deposited into tiny structures much more precisely than if injecting or painting methodologies were used [32-34].

The crystalline structures of the electrochemically deposited ruthenium oxide were characterized using an X-ray diffractometer (Fig. 14). For the samples prepared at room temperature, peaks were not observed, confirming that the ruthenium oxide possessed an amorphous structure. These data agree well with the parameters of the RuO_2 electrode prepared by Zhitomirsky [40]. Electrodeposition is similar to oxide powder processing (a wet chemical method) in that it makes use of an electrogenerated base [40-42]. For the nanocomposite, the two major peaks at 26.5° and 42.3° can be assigned to diffraction from the (002) and (100) planes of the CNTs, respectively. The fresh RuO_2 in the nanocomposite was also found to be amorphous, which is indicated by the absence of diffraction peaks (except those from the CNTs). Indeed, the results of the XRD studies also correlate with those from the SEM studies. Tightly entangled CNTs augmented with amorphous ruthenium oxide were fabricated on the 3D interdigitated fingers.

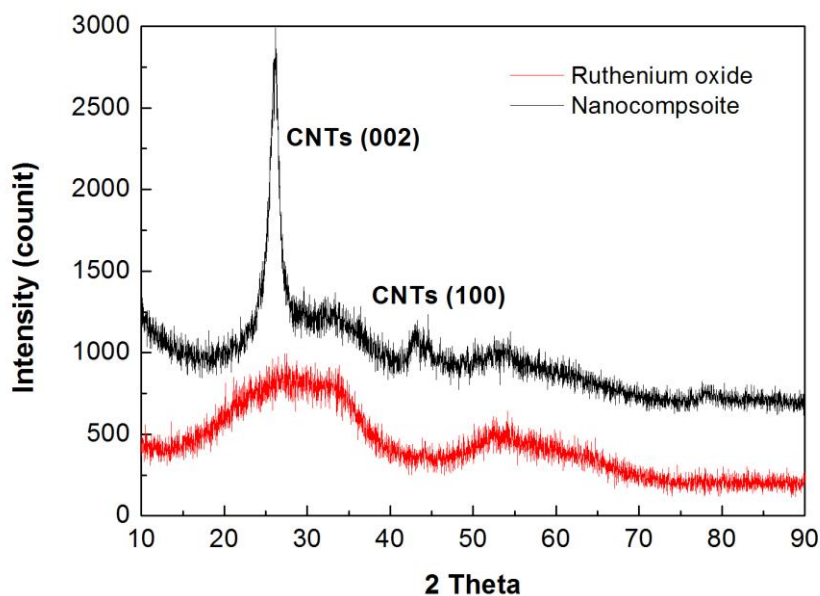
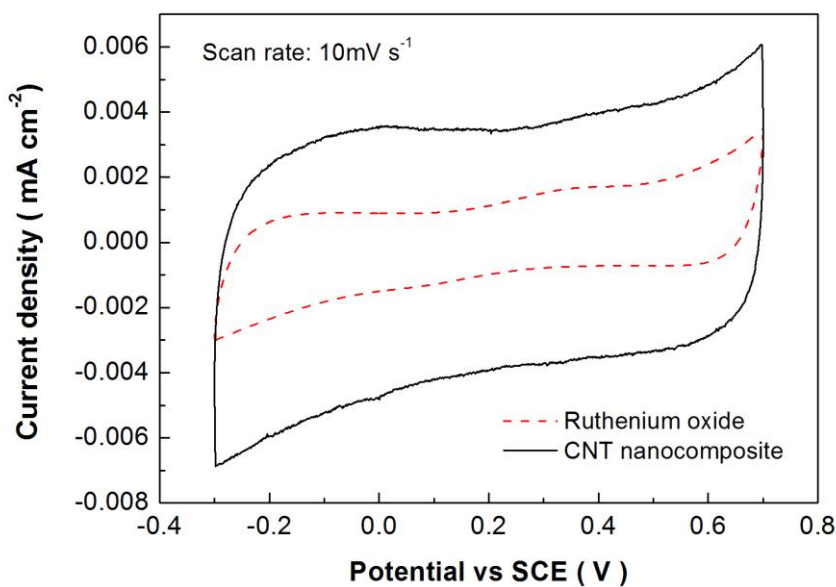


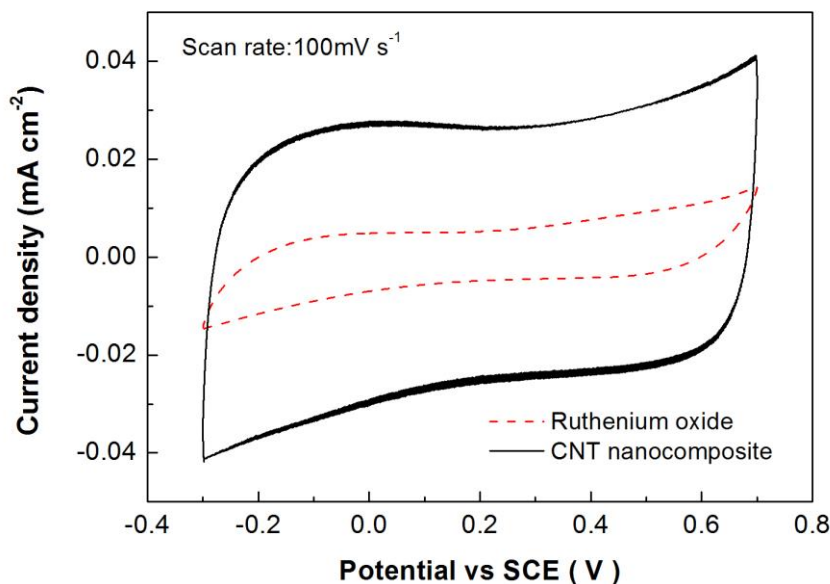
Figure 14. X-ray diffraction patterns for RuO₂ and CNTs nanocomposites.

3.2 Electrochemical testing of an individual electrode

The capacitive properties of these materials were measured using cyclic voltammetry. The CV curves for the RuO₂ and the nanocomposite with the same formation charge (40 C, 0.02 A × 2000 s) are shown in Fig. 15. Both interdigitated electrodes are identical in size (2.5mm²). To make comparison, the normalized current density (i.e., the faradic current divided by the footprint area of the electrode) was applied as a vertical axis in the normalized CV plots other than the current.



(a)



(b)

Figure 15. CV plots for RuO₂ and CNT nanocomposites at scan rates of (a) 10 mV·s⁻¹ and (b) 100 mV·s⁻¹.

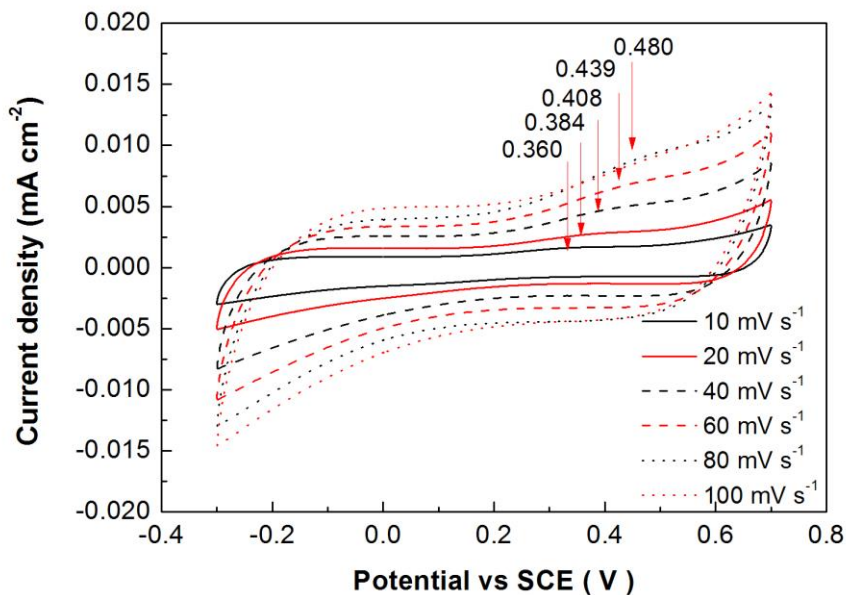
From the cyclic voltammograms, it can be seen that there are several significant differences between the two films. First, the electrode with the RuO₂ film showed a pseudocapacitive behavior, and the redox features resulted from the valence changes in the ruthenium can be found between 0.2 and 0.4 V vs. SCE. Second, the voltammogram of the RuO₂/CNT composite has a featureless and rectangular shape, and the output current of the composite film is about twice that of the RuO₂ film at same scan rate. The CNT nanocomposite is a better active electrode material than the thin RuO₂ film because of its high specific area and high electrical conductivity. The specific capacitances and energy densities of the microelectrodes can be increased by increasing the thickness of the active materials (i.e., 3D structures) in a given area. Consequently, electrochemically filling thick layers of conducting nanocomposites in 3D microstructures is an effective way to enhance the performance of micro-supercapacitors.

The potential scan rate was varied from 10 to 100 mV·s⁻¹ in order to evaluate the high-rate capability of the RuO₂/CNT composite in a potential window between -0.3 V and 0.7 V vs. SCE. The currents in the CV curves in Fig. 16 were normalized to the area of the 3D electrode. When scanned at a much higher rate of 100 mV·s⁻¹, the CV curve for the 3D electrode retained regular and quadrilateral (Fig. 16b). The anodic and cathodic voltammograms were almost mirror images of each other. This shape is indicative of ideal capacitive behavior and reveals the excellent proton and electron transport properties of the nanocomposite. The CVs of the RuO₂ microelectrodes at different scan rates were also presented in Fig. 16a for comparison. In this case, the anodic and cathodic voltammograms are separated and involve substantial anodic and cathodic over voltages and show a reversible potential at

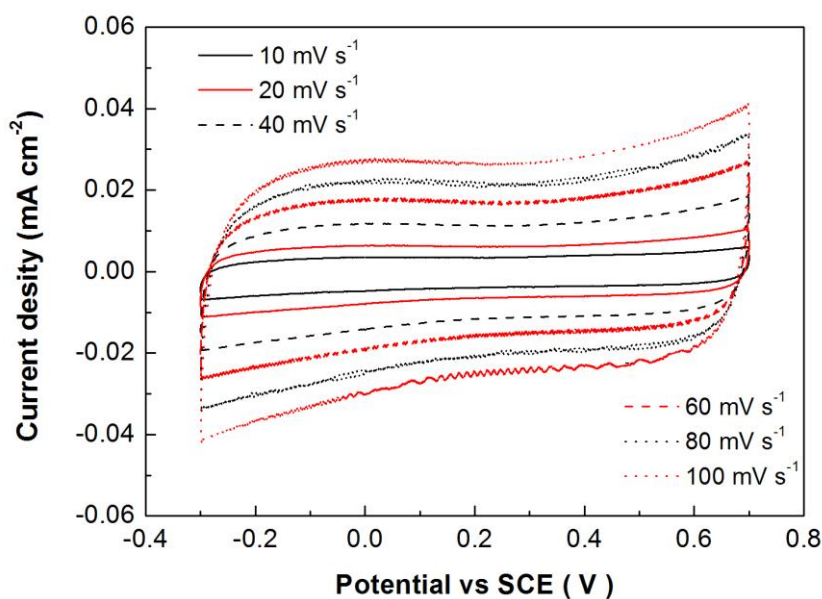
crossover, especially for high scan rates. The capacitance of an individual electrode can be calculated by integrating the current from the CV curves in a discharge half-cycle according to Eq. (1):

$$C = \frac{\int I(V)dV}{S \cdot \Delta V} \tag{1}$$

where $\int I(V)dV$ is the total voltammetric charge acquired by integrating the negative sweep in the cyclic voltammogram, S is the scan rate, and ΔV is the width of the potential window.



(a)



(b)

Figure 16. CV plots at increasing scan rates varying from 10 to 100 mV·s⁻¹ for (a) a RuO₂ microelectrode and (b) a CNT microelectrode.

The specific geometric capacitances at different scan rates were deduced by the CV data (Fig. 17). Although the nanocomposite coating was as thick as 40 μm , the specific capacitance of the composite was 208.5 $\text{mF}\cdot\text{cm}^{-2}$ at 10 $\text{mV}\cdot\text{s}^{-1}$. It decreased to 132 $\text{mF}\cdot\text{cm}^{-2}$ (by 36.6 %) at 100 $\text{mV}\cdot\text{s}^{-1}$. For comparison, the capacity loss for the RuO_2 microelectrode was approximately 55% within the same limit. The relatively lower rate of decay suggests the high rate capability of the RuO_2/CNT nanocomposite. In this study, the high specific capacitance of the RuO_2/CNT nanocomposite could be attributed to the homogeneous dispersion of nano-sized ruthenium oxide particles. The diffusion length of the ions within the pseudoactive phase is short, thus the utilization of a majority of the active materials is ensured. In addition, the 3D nanoporous RuO_2/CNT electrode may provide a large interfacial area between the the electrolyte and the active substance, creating electron conduction paths through the CNTs and facilitating facile ionic transfer within the nanopores.

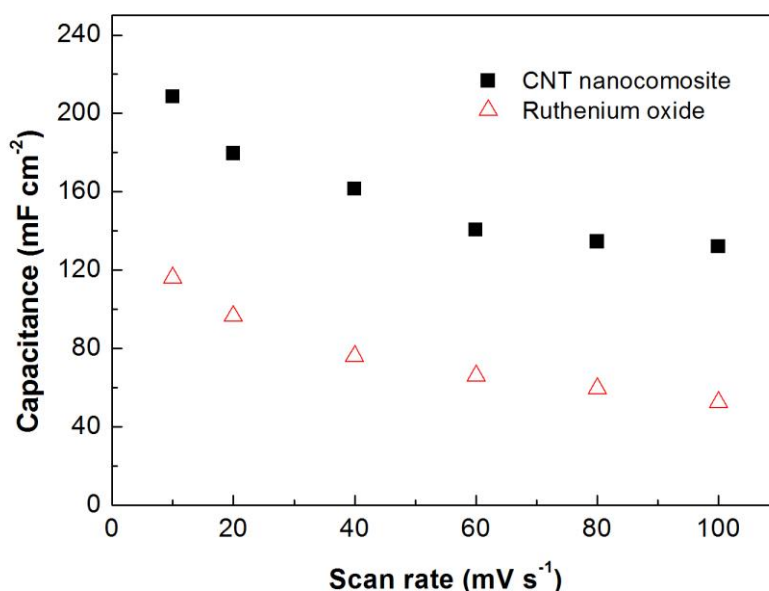
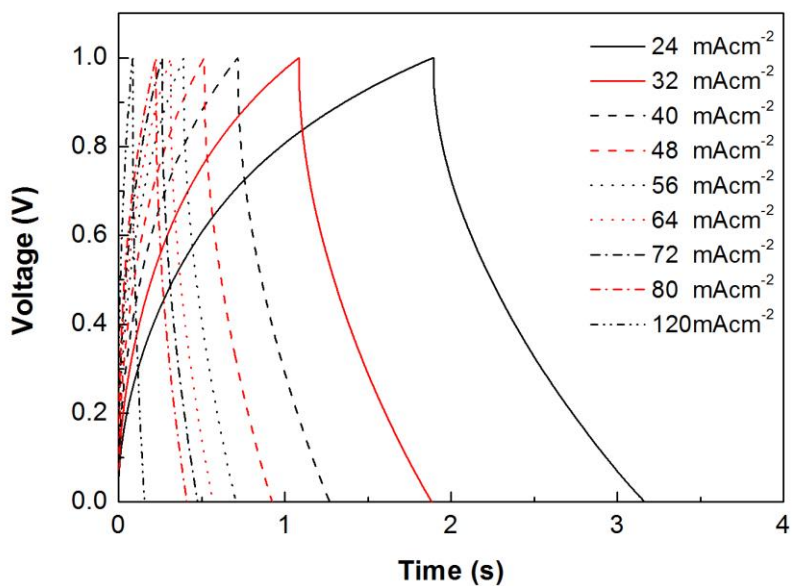


Figure 17. Specific geometric capacitances for RuO_2 and CNT microelectrodes at different scan rates.

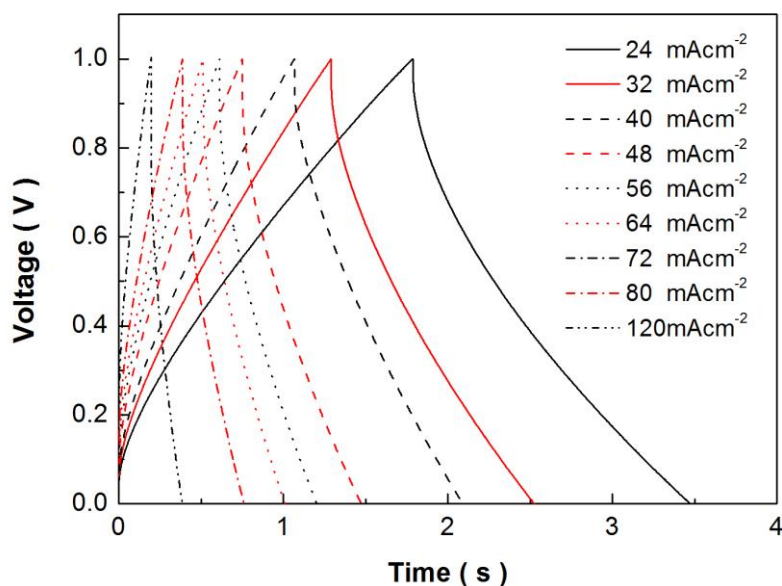
3.3 Tests of the electrochemical cell

The symmetric supercapacitor consists of two 3D microelectrodes that were electrodeposited for 2000 seconds. The device was tested in a two-electrode system in $0.1 \text{ mol}\cdot\text{L}^{-1} \text{ Na}_2\text{SO}_4$. Two electrodes with the same design specifications were simultaneously fabricated on one chip. Galvanostatic charge/discharge experiments were performed to investigate the performance of a cell containing two identical electrodes, using various current densities over a range of voltages (0-1.0 V). Charge-discharge cycles for two types of symmetric micro-supercapacitors are presented in Fig. 18a and Fig. 18b. For the capacitor composed of the CNT nanocomposite (Fig.18b), the curves showed a triangular shape with linear charge and discharge half-cycles, which is a typical supercapacitor behavior. The galvanostatic charge/discharge data were used to estimate the energy delivery efficiency from the capacity ratio between the discharge and the charge processes; it was found to be greater than

93.7%. In contrast, the curves for the capacitor composed of the RuO₂ electrode were obviously asymmetric in shape (Fig.18a), and the capacity ratio was less than 67%.



(a)



(b)

Figure 18. Galvanostatic charge and discharge curves for cells composed of (a) RuO₂ microelectrodes and (b) CNT microelectrodes at various discharge rates.

By using the linear sections of the discharge curves according to Eq. (2), the geometric capacitance of a cell can be acquired:

$$C = \frac{I \cdot \Delta t}{\Delta V \cdot A} \tag{2}$$

where I is the discharge current, A is the area of the cell (the same size as that of a single electrode), t is the discharge time, and ΔV is the potential window after the *iR* drop.

The average specific power (P) of the cell can be obtained using Eq. (3):

$$P = \frac{E}{\Delta t} = \frac{0.5C(\Delta V)^2}{\Delta t} \tag{3}$$

where E is the specific energy density of the cell. Tables 1 and 2 present the specific capacitances (C), the specific powers (P) and the specific densities (E) at different currents. As the current density increased from 8 to 120 mA·cm⁻², the average specific capacitance decreased whereas the specific power increased. For the micro device composed of the CNT nanocomposite electrodes, the specific capacitance was found to be 28.70 mF·cm⁻² at 120 mA·cm⁻², which is an exceptionally large discharge rate. At this rate, the drop in *iR* decreased with the addition of CNTs to the microelectrodes and its value was 0.266 V and 0.218 V for the RuO₂ and CNT micro-supercapacitors, respectively. The utilization of 3D microelectrodes as well as CNT nanoscale networks can enhance the performance of devices with limited footprints at high discharge rates. The specific energies and power densities of micro-supercapacitors were calculated from the discharge curves at a rate of 8 to 120 mA·cm⁻² and shown in a Ragone plot (Fig. 19). The decrease in the energy density observed as a function of increasing power density is much smaller with the CNT micro-supercapacitors. The highest energy density (25.99 mJ·cm⁻²) and the highest power density (46.92 mW·cm⁻²) were both achieved with the microdevice composed of interdigitated CNT microelectrodes.

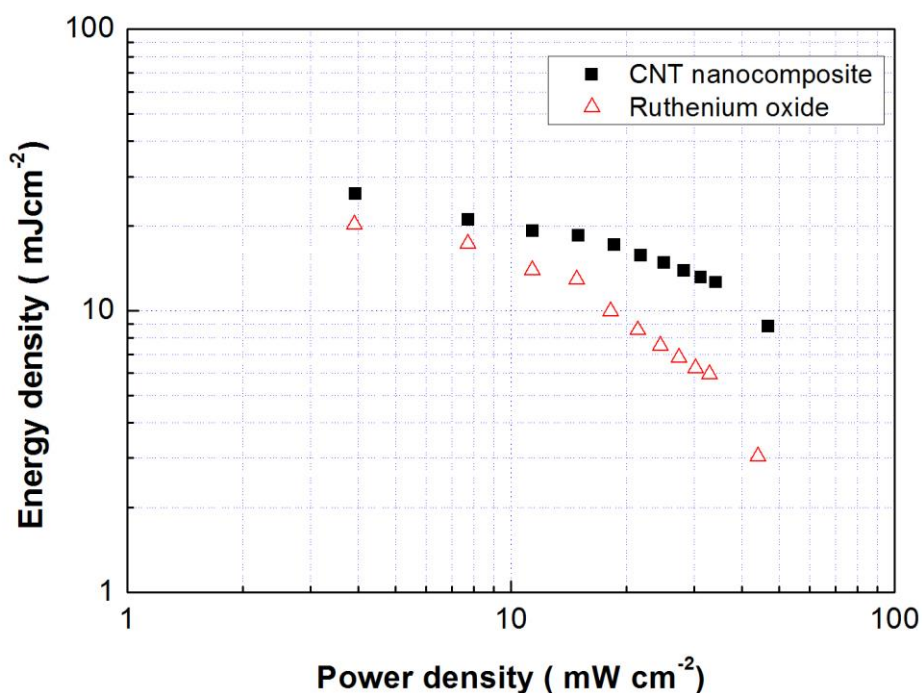


Figure 19. A Ragone plot for cells composed of RuO₂ and CNT microelectrodes.

Table 1. Properties of micro-supercapacitors composed of CNT microelectrodes operating at different discharge rates.

Current density (mA·cm ⁻²)	Discharge time (s)	Potential window (V)	Specific capacitance (mF·cm ⁻²)	Specific power (mW·cm ⁻²)	Energy density (mJ·cm ⁻²)
8	6.61	0.983	53.79	3.94	25.99
16	2.72	0.966	45.05	7.73	21.02
24	1.68	0.951	42.40	11.41	19.17
32	1.23	0.938	41.96	15.01	18.46
40	0.92	0.929	39.61	18.58	17.09
48	0.72	0.909	38.02	21.82	15.71
56	0.59	0.895	36.92	25.06	14.79
64	0.49	0.882	35.56	28.22	13.83
72	0.42	0.869	34.80	31.28	13.14
80	0.37	0.856	34.39	34.24	12.60
120	0.19	0.782	28.70	46.92	8.78

Table 2. Properties of micro-supercapacitors composed of RuO₂ microelectrodes operating at different discharge rates.

Current density (mA·cm ⁻²)	Discharge time (s)	Potential window (V)	Specific capacitance (mF·cm ⁻²)	Specific power (mW·cm ⁻²)	Energy density (mJ·cm ⁻²)
8	5.18	0.977	42.45	3.91	20.26
16	2.25	0.963	37.38	7.70	17.33
24	1.23	0.945	31.24	11.34	13.95
32	0.87	0.927	30.10	14.83	12.93
40	0.55	0.910	24.09	18.20	9.97
48	0.40	0.891	21.49	21.38	8.53
56	0.31	0.874	19.67	24.47	7.51
64	0.25	0.856	18.62	27.39	6.82
72	0.21	0.840	17.74	30.24	6.26
80	0.18	0.823	17.59	32.92	5.96
120	0.07	0.734	11.28	44.04	3.04

As shown in Table 3, the energy density and power density of our device exceed many previous reported works which adopted the pure CNT[38] and RuO₂[46][27] as the electrode material of micro supercapacitors with interdigitated structures. The power density of the CNT/RuO₂ electrode is superior to that of RuOx/GNF electrode[49].

Furthermore, a comparison of different electrode active materials for the interdigitated micro supercapacitors is presented in Table 4. It can be seen that the energy density and power density of our device are higher than many previous reported microsupercapacitors using other electrode active materials such as graphene, conducting polymer and metal oxide [47-50].

Table 3. Performance of micro supercapacitors with interdigitated 3D structures

Electrode material	Electrolyte	Device Capacitance (mF/cm ²)	Device energy (mJ/cm ²)	Device power (mW/cm ²)	Ref.
CNT	Ionic liquid	0.428	1.9	0.28	[38]
RuO ₂	1 M Na ₂ SO ₄	6.5	1.15	0.17	[44]
RuO _x	0.5 M H ₂ SO ₄	12.6	5.36	0.75	[27]
RuO _x /GNF*	0.5 M H ₂ SO ₄	55	25.2	~0.1	[45]
CNT/RuO ₂	0.1M Na ₂ SO ₄	53.79	25.99	46.92	This work

* Estimated. GNF, graphitic nanofibers.

Table 4. Performance of micro supercapacitors with different electrode materials

Electrode material	Electrolyte	Device Capacitance (mF/cm ²)	Device energy (mJ/cm ²)	Device power (mW/cm ²)	Ref.
GQD	0.5 M Na ₂ SO ₄	1.1	0.55	0.075	[46]
CDC	1 M NEt ₄ BF ₄	1.5	3	84	[47]
GP	PVA/H ₂ SO ₄	1.5	1.37	14.4	[48]
PPy	0.1 M KCl	78.35	25	1.62	[36]
PPy	0.5M NaCl	56	-	0.56	[24]
MnO ₂	1 M Na ₂ SO ₄	56.3	18	12	[49]
Co(OH) ₂	1M KOH	-	7.2	6.2	[50]
CNT/RuO ₂	0.1M Na ₂ SO ₄	53.79	25.99	46.92	This work

* Estimated. GQD, graphene quantum dot; CDC, carbide derived carbon; GP, grapheme pellet;

The high specific capacitance and exceptional rate capability of the CNT micro-supercapacitors is due to a synergistic combination of using the ideal electrode materials and assembling them to achieve a superior structural design[20]. First, when networks of CNTs are used the agglomeration of the ruthenium oxide is inhibited, allowing for a highly accessible surface area. Second, the electrochemical deposition technique is binder-free, allowing the micro-supercapacitors to handle high powers. The polymeric binders that are typically used in the fabrication of electrodes hinder their performance by increasing their resistivity and adding dead weight. Third, the high power capability of this micro-supercapacitor is enhanced by the interdigitated design of the electrodes. Because the

microelectrodes are close together, the electrolyte resistance is minimized, reducing the mean ionic diffusion pathway between the microelectrodes. Finally, the small size of the electrodes along with their side-by-side, in-plane design facilitates the diffusion of electrolyte ions over the entire electrode thickness[43].

4. CONCLUSION

This paper developed an approach for fabricating an on-chip micro-supercapacitor using MEMS technology. Ripple-like thick RuO₂/CNT films were successfully fabricated using cathodic co-deposition. The CNT network in the nanocomposite not only reduced the diffusion resistance of the electrolytes but also enhanced ion transport. The unique SU-8 microstructures on the interdigitated current collector enhanced the growth process of the ripple-like film of CNT composites. The electrochemically deposited microelectrodes showed excellent capacitive behavior, with a specific geometric capacitance of 208.5 mFcm⁻² after cathodic deposition for 2000 seconds. The performance of an on-chip supercapacitor consisting of two identical electrodes was investigated electrochemically in a Na₂SO₄ solution. The specific energy density (25.99 mJ·cm⁻²) and the specific power density (46.92 mW·cm⁻²) were obtained. MEMS techniques (e.g., UV lithography of SU-8 photoresist) are promising for constructing on-chip micro-supercapacitors.

ACKNOWLEDGMENTS

The authors acknowledge financial support from the National Natural Science Foundation of China (NNSFC) (Project No. 50905096).

CONFLICT OF INTEREST

The authors declare that they have no conflict of interest.

References

1. T. Masako, *Microelectronic Engineering*, 84 (2007)1341.
2. J. F. M. Oudenhoven, R. J. M. Vullers, R. Schaijk, *International Journal of Energy Research*, 36 (2012) 1139.
3. H. B. Radousky, H. Liang, *Nanotechnology*, 23 (2012)1.
4. S. M. M. Ehteshami, M. Asadnia, S. N. Tan, S. H. Chan, *Journal of Power Sources*, 301(2016) 392.
5. S. M. Jamil, M. H. D. Othman, M. A. Rahman, J. Jaafar, A. F. Ismail, K. Li, *Journal of the European Ceramic Society*, 35(2015)1.
6. W. Gao, N. Singh, L. Song, Z. Liu, A.L.M. Reddy, L. Ci, R. Vajtai, Q. Zhang, B. Wei, P.M. Ajayan, *Nature Nanotechnology*, 6 (2011) 496.
7. B. Hsia, M.S. Kim, M. Vincent, C. Carraro, R. Maboudian, Maboudian Roya, *Carbon*, 57 (2013) 395.
8. A. Haroun, I. Yamada, S. Warisawa, *Sensors and Actuators A: Physical*, 224(2015)87.
9. K.V. Selvan, M. S. M. Ali, *Renewable and Sustainable Energy Reviews*, 54(2016)1035.
10. R. Kotz, M. Carlen, *Electrochimica Acta*, 45 (2000) 2483.

11. A. G. Pandolfo, A. F. Hollenkamp, *Journal of Power Sources*, 157 (2006) 11.
12. C.W. Shen, X.H. Wang, S.W. Li, J.G. Wang, W.F. Zhang, F.Y. Kang, *Journal of Power Sources*, 234 (2013) 302.
13. J. Ren, L. Li, C. Chen, X. L. Chen, Z.B. Cai, L.B. Qiu, *Advanced Materials*, 25 (2013) 1155.
14. W.W. Liu, X.B. Yan, J.T. Chen, Y.Q. Feng, Q.J. Xue, *Nanoscale*, 5 (2013) 6053.
15. D. Pech, M. Brunet, T. M. Dinh, K. Armstrong, J. Gaudet, D. Guay, *Journal of Power Sources*, 230 (2013) 230.
16. P.H. Huang, D. Pech, R.Y. Lin, J.K. McDonough, M. Brunet, P.L. Tabernac, Y. Gogotsie, P. Simon, *Electrochemistry Communications*, 36 (2013) 53.
17. Y.S. Moon, D. Kim, G. Lee, S.Y. Hong, K. K. Kim, S. M. Park, J. S. Ha, *Carbon*, 81(2015)29.
18. Y. Yang, L. He, C. Tang, P. Hu, X. Hong, M. Yan, Y. Dong, X. Tian, Q. Wei, L. Mai, *Nano Research*, 9(2016) 2510.
19. N.A. Kyeremateng, T. Brousse T, D. Pech, *Nature Nanotechnology*, 12 (2017)7.
20. J. Maeng, Y. J. Kim, C. Meng, P. P. Irazoqui, *ACS applied materials & interfaces*, 8(2016) 13458.
21. C. C. B. Bofon, J. D. C. González, D. J. Thurmer, D. Grimm, M. Bauer, O.G.Schmidt, *Nano letters*, 10 (2010) 2506.
22. G. P. Xiong, C. Z. Meng, R. G. Reifenger, P. P. Irazoqui, T.S. Fisher, *Electroanalysis*, 26 (2014) 30.
23. J. H Sung, S. J. Kim, K. H. Lee, *Journal of Power Sources*, 133(2004) 312.
24. W. Sun, R. Zheng, X. Chen, *Journal of Power Sources*, 195 (2010) 7120.
25. C. C. Liu, D.S. Tsai, D. Susanti, W.C. Yeh, Y.S. Huang, F.J. Liu, *Electrochimica Acta*, 55 (2010) 5768.
26. C.B. Arnold, R.C. Wartena, K.E. Swider-Lyons, A. Pique, *Journal of the Electrochemical Society*, 150 (2003) A571.
27. S. Makino, Y. Yamauchi, W. Sugimoto, *Journal of Power Sources*, 227 (2013) 153.
28. A. Ponrouch, S. Garbarino, E. Bertin, D. Guay, *Journal of Power Sources*, 221 (2013) 228.
29. C.C. Hu, K.H. Chang, M.C. Lin, and Y.T. Wu, *Nano Letter*, 6 (2006) 2690.
30. X.F. Wang, Y.J. Yin, X.Y. Li, Z. You, *Journal of Power Sources*, 252 (2014) 64.
31. Z. S. Wu, X. Feng, H. M. Cheng, *National Science Review*, 1 (2014)277.
32. D. Pech, M. Brunet, P. L. Taberna, P. Simon, N. Fabre, F. Mesnilgrete, V. Conédéraa, H. Duroua, *Journal of Power Sources*, 195 (2010) 1266. □
33. C.W. Shen, X.H. Wang, W.F. Zhang, F.Y. Kang, *Journal of Power Sources*, 196 (2010) 10465.
34. H. Xing, X.H. Wang, C.W. Shen, S.W. Li, *Micro & Nano Letters*, 7 (2012) 1166.
35. M. Beidaghi, W. Chen, C.L. Wang, *Journal of Power Sources*, 196 (2011) 2403.
36. M. Beidaghi, C.L. Wang, *Electrochimica Acta*, 56 (2011) 9508.
37. M. Beidaghi, C.L. Wang, *International Society for Optics and Photonics (SPIE)*, Baltimore, Maryland, USA, 2012, 837708.
38. Y. Q. Jiang, Q. Zhou and L. Lin, *2009 IEEE 22nd International Conference on Micro Electro Mechanical Systems*, Sorrento, Italy, 2009, 587.
39. C.C. Liu, D.S. Tsai, W.H. Chung, K.W. Li, K.Y. Lee, Y.S. Huang, *Journal of Power Sources*, 196 (2011) 5761.
40. I. Zhitomirsky, L. Gal-Or, *Materials Letters*, 31 (1997) 155.
41. I. Zhitomirsky, *Materials Letters*, 33 (1998) 305.
42. Zhitomirsky, A. Kohn and L. Gal-Or, *Materials Letters*, 25 (1995) 223.
43. J. Y. Kim, K. H. Kim, S. H. Park, K. B. Kim, *Electrochimica Acta*, 55 (2010) 8056.
44. W. Zheng, Q. Cheng, D. Wang, C.V. Thompson, *Journal of Power Sources*, 341(2017)1.
45. J. J. Jhao, C. H. Lin, T. K. Yeh, H. C. Wu, M. C. Tsai, C.K. Hsieh, *Surface and Coatings Technology*, (2017), <http://dx.doi.org/10.1016/j.surfcoat.2017.01.006>.
46. W.W. Liu, Y.Q. Feng, X.B. Yan, J.T. Chen, J.Q. Xue, *Advanced Functional Materials*, 23(2013) 4111.

47. P. Huang, M. Heon, D. Pech, M. Brunet, P.L. Taberna, Y. Gogotsi, S. Lofland, J. D. Hettingerf, P. Simon, *Journal of Power Sources*, 225(2013)240.
48. L. Zhang, D. DeArmond, N. T. Alvarez, R. Malik, N. Oslin, C. McConnell, P. K. Adusei, Y.Y. Hsieh, V. Shanov, *Small*, 13(2017)1603114.
49. X. Wang, B. D. Myers, J.Yan, G. Shekhawat, V. Dravid, P. S. Lee, *Nanoscale*, 5(2003) 4119.
50. C.H. Chen, D. S. Tsai, W. H. Chung, K. Y. Lee, Y. M. Chen, Y. S. Huang, *Journal of Power Sources*, 205(2012)510.

© 2017 The Authors. Published by ESG (www.electrochemsci.org). This article is an open access article distributed under the terms and conditions of the Creative Commons Attribution license (<http://creativecommons.org/licenses/by/4.0/>).